Computational 3D microscopy with optical coherence refraction tomography

1. EXTENDED METHODS

A. 3D OCRT imaging

The imaging system is based on a commercial spectral domain OCT system (Bioptigen Envisu R4110 XHR SDOIS), whose illumination source is centered at 820 nm. Each single-view OCT volume consisted of $400\times400\times2048$ unaveraged voxels, covering a 3D FOV of approximately $1.3\times1.3\times1.65$ mm^3 in water, acquired at a 20-kHz A-scan rate. The OCT sample arm optics were replaced with a tube lens pair (a pair of achromatic doublets, f = 30 mm, 100 mm, Thorlabs), a protected-aluminum-coated parabolic mirror (f = 12.5 mm, Edmund Optics), and a fused silica optical dome (outer radius = 8.128 mm, inner radius = 6.858 mm, CLZ Optics). The parabolic mirror was cut in half to facilitate sample mounting and inverted so that the cut surface was facing up. The optical dome was also inverted, centered at the parabolic mirror's focus, and filled with water as the immersion medium. The power incident at the sample was $\sim$1.5 mW, after $\sim$13% loss upon reflection from the parabolic mirror. Resolution (FWHM) was characterized using sub-resolution polystyrene beads embedded in 2% agarose (w/v); the axial resolution was 2.1 µm, while the resolution in the lateral dimensions was 15.3 and 14.6 µm (x and y), enabling millimetric depths of field and lateral FOVs.

To vary the sample-incident angle, the sample arm components from the fiber output up to and including the tube lens (the probe) were mounted on two orthogonal translation stages (Zaber Technologies, Sigma Koki), which varied the 2D entry position across the aperture of the parabolic mirror. We generated 96 sampling positions so that the sample-incident unit vectors were roughly evenly distributed about the unit sphere [1] and contained approximately within the nominal angular ranges of $\pm75^\circ$ and $\pm25^\circ$ about the y- and x-axes, respectively (Fig. 1d,e). To minimize the probe's total travel distance and time while visiting all 96 positions, we used the 2-opt heuristic to find an approximate solution to the traveling salesman problem, starting at the position closest to that corresponding to normal incidence (Fig. 1d). Further, since the effective focal length (EFL) can vary as a function of incidence angle, the lateral scan range across the sample needed to be dynamically rescaled to obtain approximately the same lateral FOV at the sample. We computed this scale factor numerically under ideal conditions (i.e., perfect paraboloidal shape and alignment) and programmed the galvanometer voltages accordingly.

Of the 96 multi-view OCT volumes, we used 91 volumes that were successfully registered in the calibration step, described in the next subsection. For fair comparison, we also acquired and averaged 91 repeated OCT volumes from the normal sample-incidence angle, which were first registered to account for any drift.

B. Calibration of boundary conditions (sample-extrinsic parameters)

As described in the main text, the 3D OCRT forward model parameters can be divided into the sample-extrinsic parameters, or the calibration parameters, and the sample-intrinsic parameters, or the sample RI distribution. The calibration parameters control positions and orientations of the final sample-incident rays ($400\times400\times96$ total), which we estimated by imaging calibration phantoms consisting of 4-µm polystyrene beads sparsely distributed and embedded in 2% agarose (w/v). As a first-order estimate, we started with a parametric model, including parameters describing the parabolic mirror focal length, the 6D pose (3D position + 3D orientation) of the 2D plane of probe translation relative to the parabolic mirror, the galvanometer lateral scan amplitudes and 3D orientation (tilt and in-plane rotation), optical dome inner/outer radii and 3D position, and the relative path length difference between the sample and reference arms. All of these parameters were optimizable except for the parabolic mirror focal length and the dome radii, which were left at their nominal values.

Since this first-order estimate was insufficient due to misalignment and manufacturing imper-

fections, we included a nonparametric refinement that allowed all 96 multi-angle OCT volumes to vary individually in terms of their 6D poses, lateral scan amplitudes, and degree of non-telecentricity. In particular, the 3D positions and 2D orientations of the 400×400 rays within each OCT volume were allowed to deviate from the first-order prediction according to six up-to-fourth-order polynomial functions of the nominal 2D lateral coordinates, three for the 3D positions and three for the 2D orientations (normalization of rays to unit vectors reduces dimensionality by one).

C. Regularization terms in the computational 3D reconstruction algorithm

In addition to mean squared error (MSE), the loss function also included two Tikhonov (L2) regularization terms to aid in the estimation of the 3D RI map, one of which was a standard practice of penalizing the magnitudes of the 3D image gradients to promote smoothness, the other of which was to enforce object support. In particular, for each multi-view OCT volume, we performed a basic intensity-threshold-based segmentation of the first reflection for each A-scan, which corresponds to the tissue surface. During ray propagation (Eq. 1), the RI values along the ray trajectories are stored if the ray hasn't reached the first tissue boundary. These deviations from these RI values from that of water, the immersion medium, are squared and summed, yielding the object-support-enforcing regularization term. These three terms – the MSE and two Tikhonov regularization terms – constitute the loss, which we minimize with respect to all the calibration (sample-extrinsic) and sample-intrinsic (3D RI) parameters via the Adam optimizer [2].

D. Sample preparation

All biological samples were fixed in 4% paraformaldehyde and stored at 4° until ready for imaging. Samples were embedded in 2% agarose (w/v), mounted upside down at the mirror focus, and immersed in water to avoid having the sample dry out during data acquisition. Animal studies were performed in compliance with Duke University Institutional Animal Care and Use Committee. The PDMS microstamp sample was manually cut into a $\sim$1 mm^2 and directly immersed in water inverted.

E. Volumetric rendering of OCRT reconstructions

Intensity projection volume renderings of both 3D OCRT and OCT data (Figs. 3-6, Visualizations 1-4) were generated utilizing Amira 3D 2021 (Thermo Fisher Scientific, Inc.). Prior to rendering, background noise was separated from structural data for both reconstructed OCRT and averaged OCT volumes utilizing 3D binary morphological segmentation [3].

2. VISUALIZING THE OMMATIDIA OF THE FRUIT FLY

Interestingly, the ommatidia are less reflective than structures immediately below it and thus taking a maximum intensity projection (MIP) does not reveal them. Only when we move $\sim$8 µm away from the maximally reflective structures along vectors normal to the fly's surface do the ommatidia become apparent for OCRT, but not OCT (Fig. S5c,d).

3. GENERALIZING OCRT: ALTERNATIVE MULTI-ANGLE SYNTHESIS STRATEGIES IN ADDITION TO MEAN REFLECTIVITY

The data collection for 3D OCRT yields a 5D datacube, consisting of OCT backscattered signals as a function of 3D space and 2D orientation, $OCT(x, y, z, k_x, k_y)$. After multi-angle registration, the OCRT reconstructions were formed by averaging the backscattered signals across the angular dimensions,

$$OCRT_{mean}(x, y, z) \propto \iint_{k_x,k_y} OCT(x, y, z, k_x, k_y)\, dk_x\, dk_y, \tag{S1}$$

which is effective at reducing speckle. However, there are many other possible choices for reducing the dimensionality of the 5D datacube to 3D that would highlight alternate sample features, thereby generalizing OCRT to include new forms of contrast. Thus, Eq. S1 is a special case of a more general equation,

$$OCRT_F(x, y, z) = F_{(x,y,z,k_x,k_y)\to(x,y,z)}\Big\{OCT(x, y, z, k_x, k_y)\Big\}, \tag{S2}$$

where F is an operator that eliminates the angular dimensions, k_x and k_y. Whereas F performs the mean operation in Eq. S1, other choices of F include variance, higher-order descriptive statistics, and entropy, which would yield more information about the shape of angular backscatter distribution. The argmax function would identify the incidence angle that gives the highest backscattered signal, which would thus produce a 3D orientation map of the sample. Taking the Fourier transform across the angular dimensions before their reduction may yield structural information about the sample [4]. To identify spatial locations that exhibit a specific angular backscatter distribution profile, another option would be to use template-matching via cross-correlation or mean square error. Data-driven linear or nonlinear dimensionality-reduction strategies could also be leveraged to collapse the angular dimensions, such as principal component analysis (PCA), t-distributed stochastic neighborhood embedding (t-SNE) [5], or neural networks. Even more generally, in addition to k_x and k_y, F could also operate along space and time (x, y, z, t). Thus, F would also include spatial convolutions and temporal variance-based approaches, such as OCT angiography (OCTA) [6] and dynamic OCT [7].

The wealth of options for mapping the 5D datacube to the 3D OCRT reconstruction opens the door to many future studies that could expand the utility and applicability of 3D OCRT. To demonstrate this potential, we investigated the case where F computes the angular variance,

$$\begin{aligned} OCRT_{var}(x,y,z) &\propto \iint_{k_x,k_y} \Big(OCT(x,y,z,k_x,k_y) - OCRT_{mean}(x,y,z) \Big)^2 \, dk_x \, dk_y, \\ &= \iint_{k_x,k_y} OCT^2(x,y,z,k_x,k_y) \, dk_x \, dk_y - OCRT^2_{mean}(x,y,z). \end{aligned} \tag{S3}$$

where, in practice, we used the second line of Eq. S3, as this expanded form only requires two mappings from the OCT datacube space to the OCRT reconstruction space (i.e., $OCT \rightarrow OCRT_{mean}$ and $OCT^2 \rightarrow OCRT^2$), thus allowing us to directly apply our moving average-based reconstruction algorithm described in the Methods section. The first line of Eq. S3 would have required us to perform an extra inverse mapping step from OCRT space to OCT space (in addition to two forward mappings). A variance-based OCRT reconstruction would highlight anisotropically backscattering structures, such an oriented flat surface. For example, an ideal spherical particle would yield no variance signal, as the backscattered signal would be independent of incidence angle. However, an ideal mirror would yield a high variance signal, as it strongly retroreflects at normal incidence and doesn't retroreflect at other incidence angles. A good example of orientationally-sensitive structures are those in Henle's fiber layer of the retina [8], whose reconstructed OCRT signal could be attenuated if we just use angular averaging (Eq. S1).

Fig. S6 compares 2D cross-sections of the standard-deviation-based 3D OCRT reconstructions of the zebrafish and mouse samples to those of the conventional mean-based 3D OCRT reconstructions. As expected, the standard-deviation-based reconstructions highlight oriented structures, such as the reticular structures within the zebrafish yolk sac, muscle fibers surrounding the mouse esophagus, and the boundaries of the cartilage plates in the mouse trachea, including to some extent the lacuna or the small cavities within the cartilage.

REFERENCES

1. M. Deserno, "How to generate equidistributed points on the surface of a sphere," If Polym. (Ed.) **99** (2004).
2. D. P. Kingma and J. Ba, "Adam: A method for stochastic optimization," arXiv preprint arXiv:1412.6980 (2014).
3. R. M. Haralick, S. R. Sternberg, and X. Zhuang, "Image analysis using mathematical morphology," IEEE transactions on pattern analysis machine intelligence pp. 532–550 (1987).
4. A. Wax, C. Yang, V. Backman, K. Badizadegan, C. W. Boone, R. R. Dasari, and M. S. Feld, "Cellular organization and substructure measured using angle-resolved low-coherence interferometry," Biophys. J. **82**, 2256–2264 (2002).
5. L. Van der Maaten and G. Hinton, "Visualizing data using t-SNE." J. Mach. Learn. Res. **9** (2008).
6. R. K. Wang, S. L. Jacques, Z. Ma, S. Hurst, S. R. Hanson, and A. Gruber, "Three dimensional optical angiography," Opt. Express **15**, 4083–4097 (2007).
7. J. Scholler, K. Groux, O. Goureau, J.-A. Sahel, M. Fink, S. Reichman, C. Boccara, and K. Grieve,

"Dynamic full-field optical coherence tomography: 3d live-imaging of retinal organoids," Light. Sci. & Appl. **9**, 1–9 (2020).
8. B. J. Lujan, A. Roorda, R. W. Knighton, and J. Carroll, "Revealing Henle's fiber layer using spectral domain optical coherence tomography," Investig. Ophthalmol. & Vis. Sci. **52**, 1486–1492 (2011).
9. K. C. Zhou, R. Qian, S. Degan, S. Farsiu, and J. A. Izatt, "Optical coherence refraction tomography," Nat. Photonics **13**, 794–802 (2019).

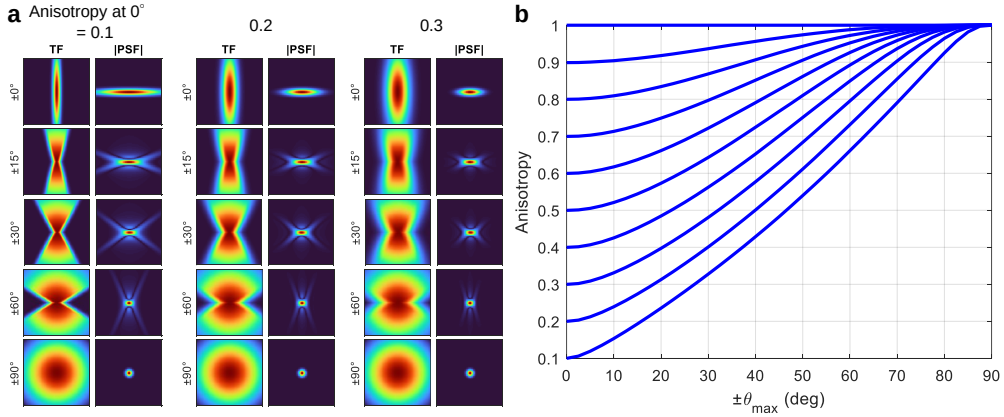

Fig. S1. Theoretical resolution enhancement as a function of angular coverage. Resolution is quantified using the full width at half maximum (FWHM) criterion. (a) Simulated transfer functions (TFs) and point-spread functions (PSFs) as a function of angular coverage. The three columns correspond to different resolution anisotropy conditions (axial-to-lateral resolution ratio = 0.1, 0.2, or 0.3). (b) Axial-to-lateral FWHM ratio of synthesized PSF as a function of angular coverage; each curve corresponds to a different initial anisotropy. These curves differ from those of our previous theoretical predictions [9], which used a different, more conservative resolution criterion.

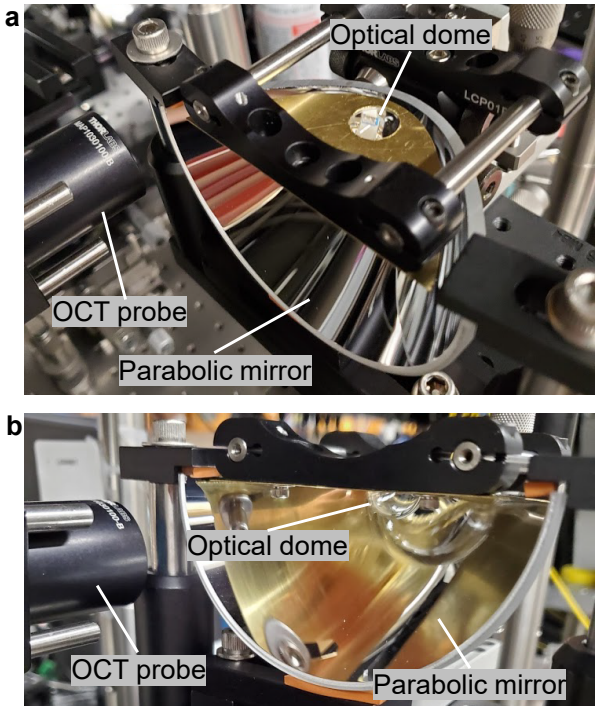

Fig. S2. (a,b) Photographs of the 3D OCRT setup, depicting the OCT probe, which is laterally scanned, the half parabolic mirror, and the optical dome.

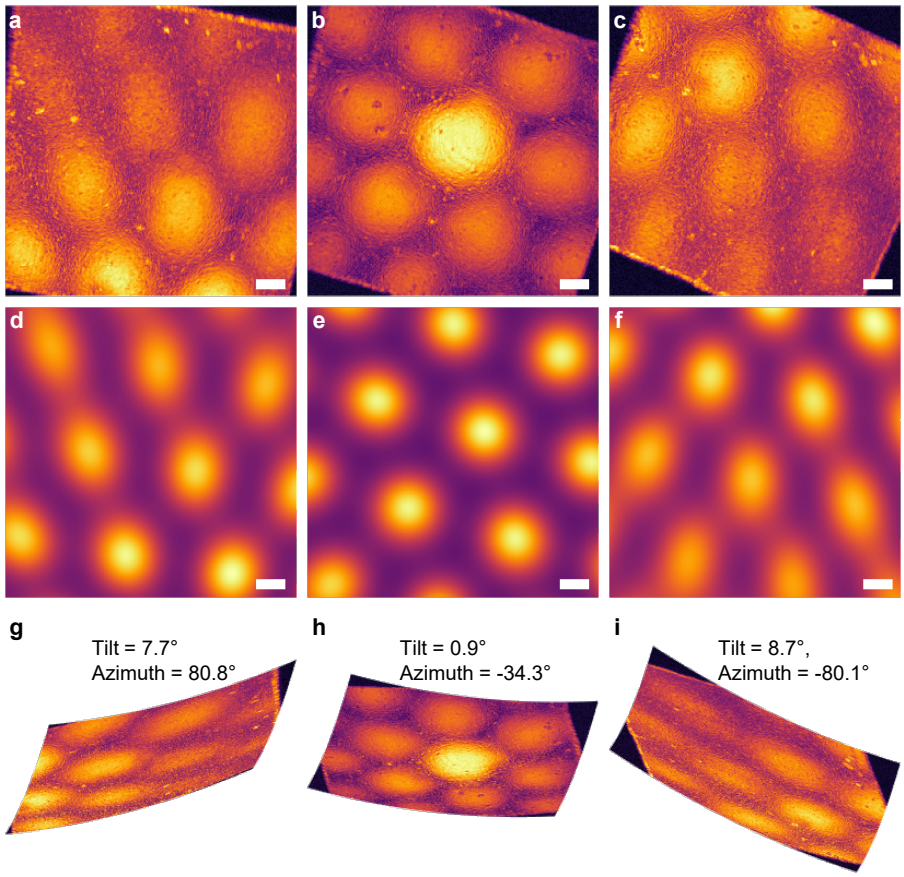

Fig. S3. OCT simulations of the interference artifacts of the 5-µm microstamp sample under different tilts match experimental results. (a-c) en face projections of the OCT volumes acquired under three different tilt angles. (d-f) Simulated en face OCT images based on fitting the microstamp surfaces to paraboloids to estimate the local tilts and surface curvature, plotted in (g-i) with a 3× exaggeration in z. The mean orientation of the surface is specified in spherical coordinates, where tilt is with respect to the z-axis. Both view angle and non-telecentricity contribute to the interference artifacts. Scale bars, 200 µm.

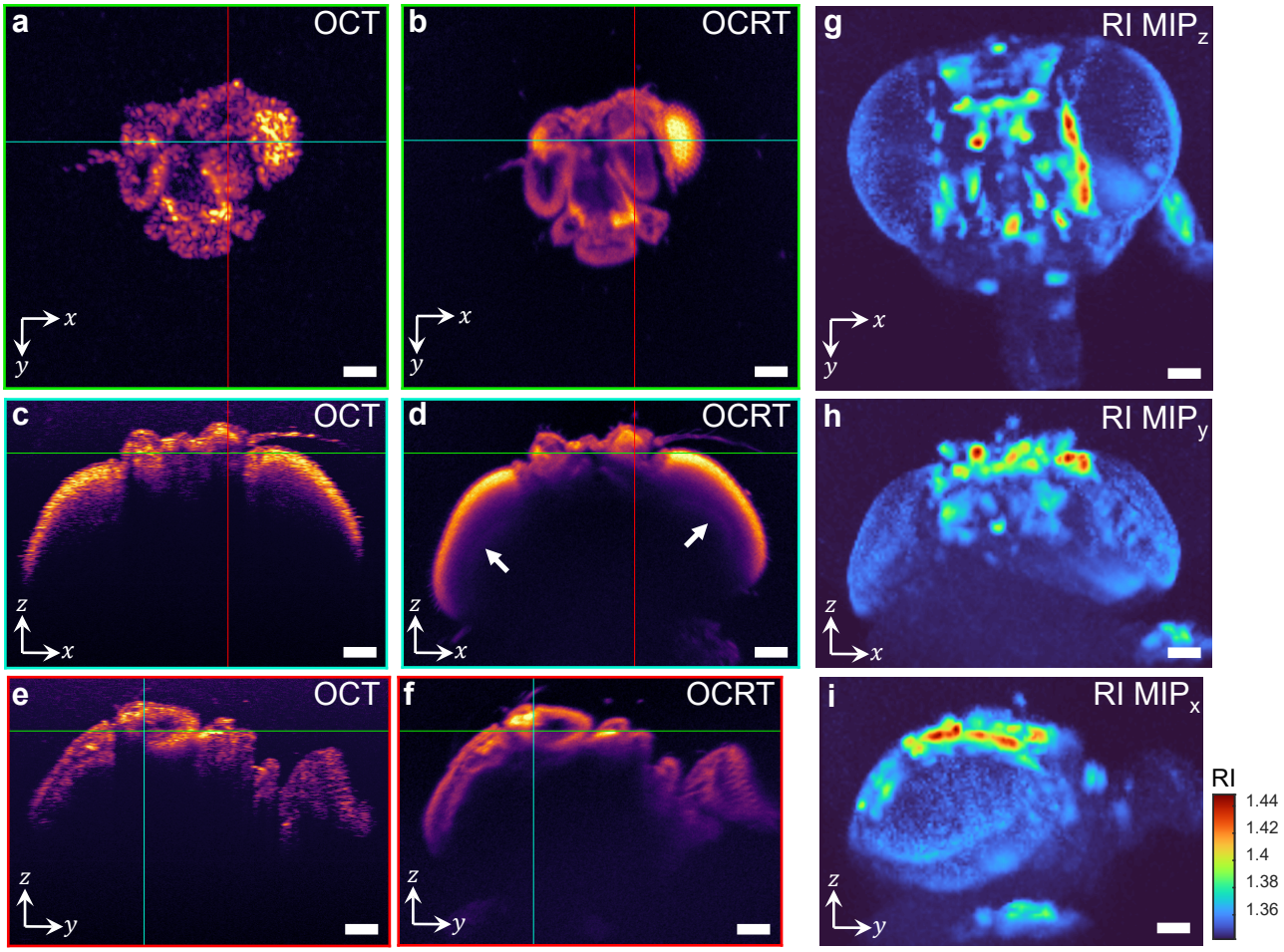

Fig. S4. Additional fruit fly results. (a-f) Comparisons of cross-sections of conventional OCT and 3D OCRT reconstruction of the fruit fly head across in an xy plane (a-b), xz plane (c-d), and yz plane (e-f). Borders are color-coded to match the cross-section locations, indicated by horizontal and vertical lines in (a-f). OCRT enhances penetration depth, revealing deep sub-surface structures (arrows in (d)). (g-i) Maximum intensity projections (MIPs) of the 3D RI map reconstruction of the fruit fly head across z (g), y (h), and x (i). Scale bars, 100 µm.

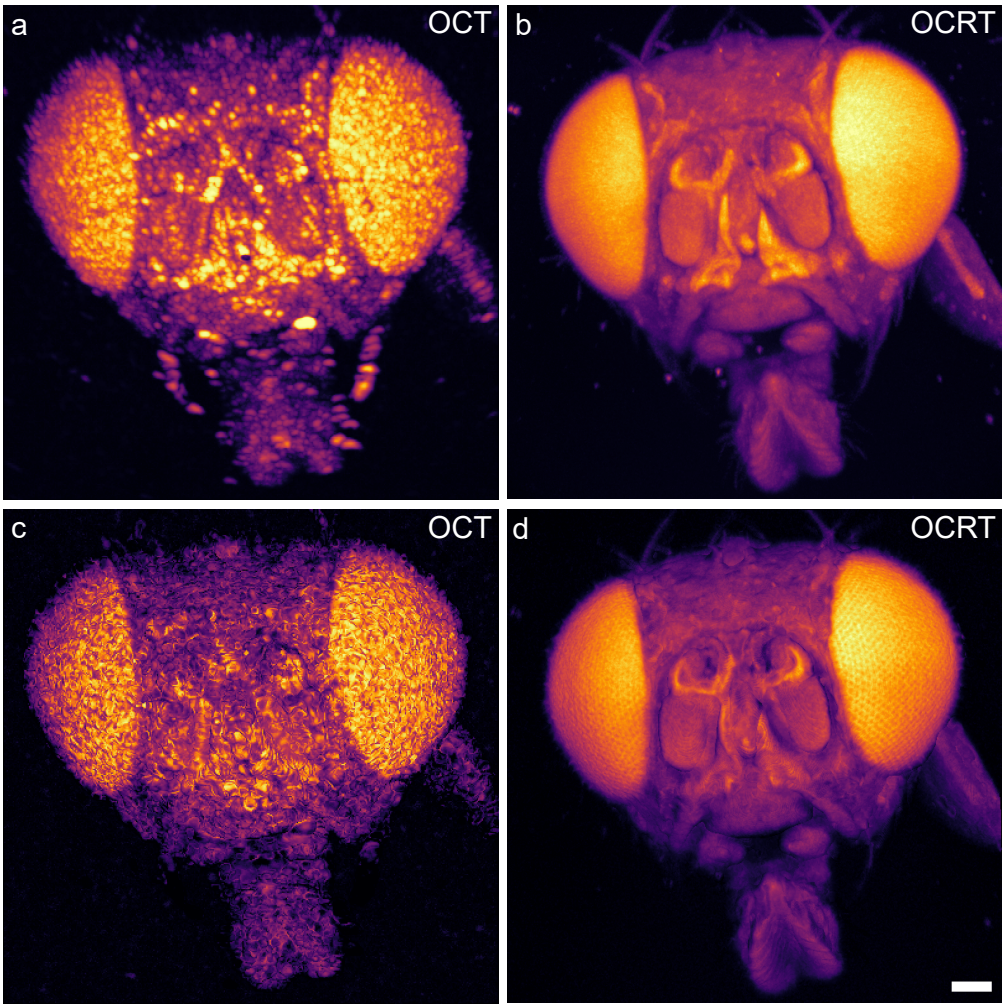

Fig. S5. Maximum intensity projection (MIP) comparison of conventional OCT and 3D OCRT reconstruction of a fruit fly head. (a) en face MIP (z points into the page) of OCT. (b) en face MIP of the 3D OCRT reconstruction. (c,d) intensity values $\sim$8 µm away, along the surface normals, from the positions corresponding to the maximum intensity for each lateral pixel. At these positions, the micro lenslets (ommatidia) are more obvious in OCRT (zoom into the plot). (a) and (c) are histogram-matched to (b) and (d), respectively. Scale bar, 100 µm.

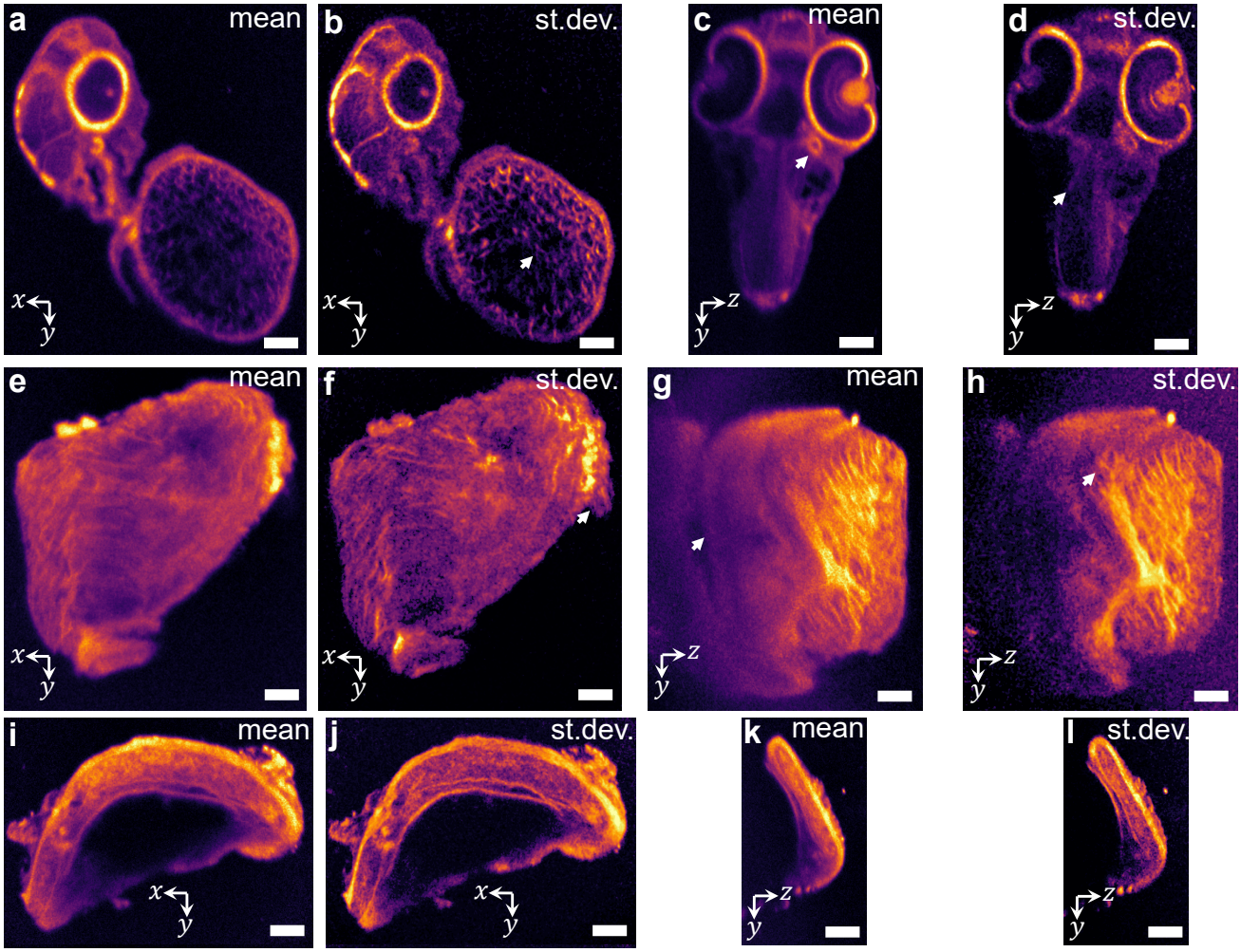

Fig. S6. Alternative multi-angle synthesis strategies lead to new contrast mechanisms. The 2D cross-sections of the 3D OCRT reconstructions in (a,c,e,g,i,k) were computed based on the mean OCT reflectivity across all angles, while those in (b,d,f,h,j,l) were computed based on the standard deviation (st. dev.) of the OCT reflectivity across all angles. Arrowheads point out a few example features that are highlighted in the mean- or st. dev.-based reconstruction more so than in the other. Scale bars, 100 µm.